1 **OBS noise reduction from horizontal and vertical**

2 **components using harmonic-percussive separation**

3 **algorithms**

4 Zahra Zali[1,2], Theresa Rein[1], Frank Krüger[1], Matthias Ohrnberger[1], Frank Scherbaum[1]

5 [1]University of Potsdam, Institute of Geosciences, Karl-Liebknecht-Str. 24-25, 14476 Potsdam, Germany

6 [2]GFZ German Research Centre for Geosciences, Potsdam, Germany

7 *Correspondence to*: Zahra Zali (zali@uni-potsdam.de)

8

9 Zahra Zali: Campus Golm, Building 29, Room 2.48, Karl-Liebknecht-Str. 24-25, 14476 Potsdam, Germany

10 (zali@uni-potsdam.de)

11 Theresa Rein: Campus Golm, Building 27, Room 0.43, Karl-Liebknecht-Str. 24-25, 14476 Potsdam,

12 Germany (theresa.rein@uni-potsdam.de)

13 Frank Krüger: Campus Golm, Building 27, Room 1.36, Karl-Liebknecht-Str. 24-25, 14476 Potsdam,

14 Germany (Frank.Krueger@geo.uni-potsdam.de)

15 Matthias Ohrnberger: Campus Golm, Building 27, Room 1.37, Karl-Liebknecht-Str. 24-25, 14476

16 Potsdam, Germany (Matthias.Ohrnberger@geo.uni-potsdam.de)

17 Frank Scherbaum: Campus Golm, Building 29, Room 1.52, Karl-Liebknecht-Str. 24-25, 14476 Potsdam,

18 Germany (Frank.Scherbaum@geo.uni-potsdam.de)

19

Abstract

Records from ocean bottom seismometers (OBS) are highly contaminated by noise, which is much stronger compared to data from most land stations, especially on the horizontal components. As a consequence, the high energy of the oceanic noise at frequencies below 1 Hz considerably complicates the analysis of the teleseismic earthquake signals recorded by OBSs.

Previous studies suggested different approaches to remove low-frequency noises from OBS recordings, but mainly focused on the vertical component. The records of horizontal components, crucial for the application of many methods in passive seismological analysis of body and surface waves, could not be much improved in the teleseismic frequency band. Here we introduce a noise reduction method, which is derived from the harmonic-percussive separation algorithms used in Zali et al., (2021) in order to separate long-lasting narrowband signals from broadband transients in the OBS signal. This leads to significant noise reduction of OBS records on both the vertical and horizontal components and increases the earthquake signal-to-noise ratio (SNR) without distortion of the broadband earthquake waveforms. This is demonstrated through tests with synthetic data. Both SNR and cross-correlation coefficients showed significant improvements for different realistic noise realizations. The application of denoised signals in surface wave analysis and receiver functions is discussed through tests with synthetic and real data.

1 Introduction

Ocean bottom seismometer recordings are generally difficult to analyze, because the noise level is usually much higher compared to land stations. At frequencies below 1 Hz, the effect of the ocean noise often dominates the data and hinders the seismological analysis (e.g. Webb et al., 1991; Crawford, 1994). Signals of interest, i.e. transient signals, especially from teleseismic events can be masked by the oceanic noise. Here, the horizontal components are most strongly contaminated by low frequency noise. To illustrate the noise on OBS data, we exemplary show the records of the station D10 of the DOCTAR array (see Fig. 1 and Fig. S1). Various studies tried to identify and characterize the different sources of noise recorded at the ocean bottom (e.g. Webb, 1998; Crawford & Webb, 2000; Corela, 2014; Stähler et al., 2018; Essing et al., 2021; An et al., 2021). In our study, we focus on noise sources that especially affect teleseismic horizontal recordings in the frequency band of 0.02–2 Hz. Generally, the dominant natural noise signals in the oceanic environment are secondary oceanic microseisms (Rayleigh/Scholte waves at the ocean bottom) caused by the interaction of wind-generated water waves, infragravity waves (compliance noise) as well as tilt noise; the latter originates from the turbulent interaction between currents and the instrument (e.g. Crawford et al., 1998; Corela, 2014). Primary oceanic microseism originates from the interaction of water waves incident at steep coastlines and/or rough seafloor (Hasselmann, 1963; Webb, 1998; Bell et al., 2015). Its spectral peak is around 0.07 Hz (Friedrich et al. 1998) in the Northern Atlantic. The secondary microseism has frequencies above 0.1–0.25 Hz, with a highest spectral peak around 0.14 Hz (Friedrich et al., 1998, Fig. 1). It is caused by wind or swell waves propagating in opposite directions. The primary and secondary microseisms affect both the vertical and horizontal seismometer components, whereas the compliance noise

57 is solely observed on the vertical component and the hydrophone. Compliance noise, dominant in the
58 frequency band of 0.01–0.04 Hz, is only significant if its wavelength exceeds the water depth (Crawford et
59 al., 1998; Crawford & Webb, 2000; Bell et al., 2015).

60 Below frequencies of 0.01 Hz and 0.1 Hz, the vertical and especially the horizontal components, are highly
61 contaminated by tilt noise generated by ocean bottom currents (Webb, 1998; Crawford& Webb, 2000;
62 Stähler et al., 2018, Fig. 1). The tilt noise level increases with signal period (see Fig. 1). The ocean bottom
63 currents in many regions of the oceans are mostly driven by tidal force and often create a signal with
64 strongest amplitudes below 1 Hz, appearing every 6–12 hours (e.g. Brink, 1995; Crawford & Webb, 2000;
65 Ramakrushana Reddy et al., 2020; Essing et al., 2021). The ocean bottom currents passing the instrument
66 create local eddy currents, deform the seafloor beneath the sensor and tilt the whole instrument frame, to
67 which the seismometer is fixed (e.g. Duennebier & Sutton, 1995; Webb, 1998; Romanowicz et al., 1998;
68 Crawford & Webb, 2000; Corela, 2014; Stähler et al., 2018). Since the noise sources often act at
69 frequencies of teleseismic earthquakes, it is crucial to improve the signal-to-noise ratio (SNR) on OBS
70 recordings for the analysis of the Earth's crustal and mantle structure. Various studies discussed the
71 improvement of OBS recordings through different approaches, either by suggesting a better OBS
72 instrument design (Stähler et al., 2018, Corela, 2014, Essing et al., 2021), or by removing significant
73 amounts of the noise from the contaminated data by signal processing (Crawford & Webb, 2000, Bell et al.,
74 2015, Janiszewski et al., 2019). Our study follows the latter approach.

75 Crawford and Webb (2000) developed a method to remove noise from the vertical OBS component.
76 Calculating the linear transfer function between the horizontal and the vertical component allows
77 estimating the tilt noise which then can be subtracted from the vertical component. Pressure data measured
78 in parallel to the seismometer recordings allow reducing the influence of infragravity waves on the vertical
79 seismometer component recordings. For better results, Bell et al. (2015) propose to first rotate the
80 horizontal components into the direction of the highest coherence between the horizontal and vertical
81 component before calculating the linear transfer functions. The mentioned methods solely improve the
82 SNR on the vertical component whereas the noise contamination on horizontal components is often larger.
83 Other recent studies attempted to reduce noise also on the horizontal components (Mousavi and Langston,
84 2017; Zhu et al., 2019; An et al., 2021; Negi et al., 2021). An et al. (2021) tried to reduce the noise on the
85 horizontal components by applying the reversed procedure of Bell et al. (2015). Rotation of one horizontal
86 component into the direction of the principle noise indeed results in an improvement of the orthogonal
87 horizontal component, but the other horizontal component became noisier (An et al., 2021). Results of a
88 recent study applying a polarization filter to reduce the noise on all components show strong changes of the
89 broadband waveforms (Negi et al., 2021). The automatic noise-attenuation method developed by Mousavi
90 and Langston (2017) is a time-frequency denoising algorithm using the wavelet transform and
91 synchrosqueezing. It can be either used to keep the signal and remove the noise or vice versa. The
92 decomposition method DeepDenoiser from Zhu et al. (2019) is based on a deep neural network.
93 DeepDenoise decomposes the waveform into signal and noise in the time-frequency domain. The latter

94 methods, both improve the SNR, but mainly focus on local and regional earthquake detection. They result
95 in changes in the waveform shape if the noise amplitude directly ahead of the signal is significant in
96 comparison to the signal amplitude in a specific frequency. However, the analysis of undistorted broadband
97 waveforms on the horizontal components is crucial for many passive seismological structure analysis
98 methods, e.g. the calculation of receiver functions or surface wave dispersion and polarization analysis.
99 Here we introduce a method, inspired from music information retrieval (MIR) research, which is adapted to
100 seismological data and is used for noise reduction on both, the vertical and the horizontal components.
101 Seismic waveforms and acoustic signals generated by musical instruments are similar in some aspects
102 (Schlindwein et al., 1995; Johnson and Watson, 2019). The extensive research in the field of music
103 information retrieval has resulted in advances (e.g., Müller, 2015) that may be useful in seismic signal
104 processing as well. Exploiting the idea of harmonic-percussive separation (HPS) in MIR, Zali et al. (2021)
105 developed an algorithm to separate harmonic volcanic tremor from earthquakes in seismic waveforms. In
106 the present study we use this algorithm after some modifications in order to separate 'harmonic' (long-
107 lasting narrowband signals) and 'percussive' (broadband transients) components of an OBS data set aiming
108 at noise reduction and retrieval of clearer broadband earthquake waveforms. Throughout this study we will
109 make use of the term noise for any signal other than earthquake signal in the data set. In the context of OBS
110 noise reduction using HPS algorithms, percussive components correspond to earthquake signals and
111 harmonic components correspond to noise signals. The long-duration OBS noise signals that last a few
112 hours to days (depending on the noise type) with a restricted frequency range contrasts with transient
113 seismic signals such as earthquakes with a wider range of frequencies.
114 The algorithm introduced in Zali et al., (2021) is a combination of two HPS approaches that leads to the
115 desired signal separation. Here we also use the two approaches in sequence in order to separate different
116 type of noise signals from the earthquake signals. In the first step we use a similarity matrix (Rafii and
117 Pardo, 2012; Rafii et al., 2014) to separate monochromatic and harmonic noises. In the second step we use
118 median filtering (FitzGerald, 2012) in order to separate the remaining narrow-band signals. With this two-
119 step approach we can separate and remove much of the OBS noise contamination from the earthquake
120 signals.
121

2 Data

123 In this study, we discuss the noise recorded by a LOBSTER (Longterm OBS for Tsunami and Earthquake
124 Research) OBS instrument from the DEPAS pool, which is equipped with a Güralp CMG-40T seismometer
125 and a MCS (Marine compact seismic) recorder (for technical specification see Stähler et al., 2018). We
126 show data recorded during the DOCTAR deployment, using DEPAS-LOBSTERs, located around the
127 Gloria Fault in the Northern Atlantic. Twelve DEPAS-LOBSTERs form the array. They were deployed
128 between 2011-2012 and recorded the data with a sampling frequency of 100 Hz (Hannemann et al., 2016;
129 Hannemann et al., 2017).

130 We observed a continuous harmonic signal at a frequency of 0.04 Hz, partially with one or two overtones
131 on a subset of the array (see Fig. 1). This signal was observed on 30% of the stations from the DOCTAR
132 project (e.g., Hannemann et al, 2016, Hannemann et al., 2017) and on 43% of the stations from the
133 KNIPAS project (Schlindwein et al., 2018), both using the mentioned DEPAS-LOBSTER design. We
134 cannot identify the source of this signal yet, but based on its continuity, we assume an electronic source
135 from the instrument itself.

136 The hydrophone and especially the horizontal components are highly affected by the strumming of the
137 head-buoy, which is attached to the DEPAS-LOBSTER frame causing a 'current-induced harmonic tremor
138 signal' (Stähler et al., 2018; Essing et al., 2021, Fig. 1). These 'tremor events' last over up to 4 hours and
139 appear every 6–12 hours. These presumably tidal-driven tremor events are harmonic signals with a
140 fundamental period of 0.4–1 s and various overtones (1–10 Hz) (Stähler et al., 2018; Essing et al., 2021,
141 Fig. 1). Regarding the frequency band, 'tremor events' mainly affect the analysis of teleseismic body
142 waves, especially on the horizontal component (Fig. 1).

143

144 **3 Noise reduction methodology**

145

146 **3.1 Harmonic-percussive separation (HPS)**

147

148 Harmonic-percussive separation refers to the problem of decomposing a signal into its harmonic and
149 percussive components. This topic has received much attention in recent years (Rafii et al., 2018) and has
150 numerous applications in the field of MIR and musical signal processing.

151

152 Within a general context harmonic signals show an overtone structure in the spectral domain. We call
153 overtones one or more clear narrow-banded frequency peaks being integer multiples of the fundamental
154 frequency (the first frequency peak in the spectrum). Harmonic signals have a relatively stable behavior
155 over time and can be identified in a Short Time Fourier Transform (STFT) spectrogram by horizontal
156 structures referred to constant frequencies along the time axis.
157 In contrast, percussive signals form vertical structures in a STFT spectrogram that contain energy in a wide
158 range of frequencies. Therefore it is a straightforward strategy in most HPS algorithms to try to separate the
159 horizontal structure from the vertical structure in the spectrogram corresponding to harmonic and
160 percussive components, respectively. The horizontal lines in the spectrogram could correspond to either
161 harmonic signals or monochromatic signals.

162

163 **3.2 HPS using median filtering (MED)**

164

165 One of the simplest and fastest HPS approaches is median filtering (FitzGerald, 2010). For simplification
166 we name this algorithm as MED in this study. Median filters are usually used to remove noise from an
167 image or a signal. Using a median filter a sample will be replaced by the median of neighboring samples
168 within a window of a specific length (The specific length is the kernel size of the median filter). The entire
169 signal is processed using a sliding window analysis. Within the HPS, two median filters are applied to the
170 amplitude of the STFT spectrogram of a signal. One median filter is performed along the time axis of the
171 spectrogram to suppress percussive events and enhance harmonic components. Another median filter is
172 applied along the frequency axis in order to enhance percussive events and suppress harmonic components.
173 The two resulting spectrograms are then subsequently used to create two masks, which are applied to the
174 original signal spectrogram separately to generate two spectrograms of harmonic and percussive
175 components, respectively. For creating the harmonic and percussive signals in the time domain the phase of
176 the original signal is added to each spectrogram and the time domain signals are reconstructed using the
177 inverse STFT.
178
179 **3.3 HPS using the similarity matrix (SIM)**
180
181 Another powerful approach in HPS proposed by Rafii & Pardo (2012) is based on calculating a similarity
182 matrix. We name this algorithm as SIM here. This approach is a repetition-based separation, which
183 identifies repeating elements in the spectrogram by looking for similarities by means of a similarity matrix.
184 Within the SIM algorithm, first similar time frames in the spectrogram are identified through a similarity
185 matrix. Then a median filter is applied only to the frames identified as similar to constitute the repeating
186 spectrogram model that corresponds to harmonic components. The non-repeating spectrogram that
187 corresponds to the percussive component of the data is obtained by subtracting the repeating spectrogram
188 from the original spectrogram. For creating repeating and nonrepeating signals in the time domain, the
189 phase of the original signal is added to each spectrogram and the time domain signals are reconstructed
190 using the inverse STFT. Details of this approach are discussed in the following section.
191
192 **3.4 HPS noise reduction algorithm for OBS data**
193
194 The motivation for using HPS for noise reduction of OBS data stems from the different characteristic of
195 earthquake and OBS noise signals as described in section 2. Earthquakes are broadband transient signals,
196 while the signals of OBS noises are more narrow-band compared to earthquakes. We combine two
197 modified HPS algorithms to separate those signals in a two-step procedure. We divide the frequency
198 content of the signal into two frequency ranges; MED frequency range covers the frequency range between
199 0.1 to 1 Hz whereas SIM frequency range contains the complementary frequency range, i.e. all frequencies
200 except the band between 0.1 and 1 Hz. Then two different algorithms are applied to these ranges,
201 respectively. In the first step, we use the SIM algorithm and separate only harmonic or monochromatic

202 signals from the original records in the SIM frequency range. The reason is related to the frequency content
203 of the noise and earthquake signals and how the SIM algorithm separates them. For a better understanding,
204 we first explain how the algorithm works and then present more detail about this selection. In the second
205 step, to reduce noise from MED frequency range we apply MED. There we target harmonic (or
206 monochromatic) as well as narrow-band signals with gliding frequencies named as current-induced
207 harmonic tremor signal in section 2. The overall schematic diagram of our HPS noise reduction algorithm
208 along with an example is shown in Fig. 2.
209 The SIM algorithm is explained in the following: From the original OBS record SO (SO represents the
210 original restituted OBS signal) we derive the STFT named X being a complex-valued spectrogram.
211 The complex-valued spectrogram X is separated into its amplitude and phase components using Eq. 1.
212

$$X = V * exp(1j * \varphi), \qquad\qquad (1)$$

213

214 where φ is the phase of X, $V = |X|$ is the amplitude of X and j is the imaginary unit.
215 All of the spectrogram modifications will be applied to the amplitude spectrogram V. The cosine similarity
216 (the similarity between two vectors of an inner product space) between the STFT time frames is calculated
217 through the multiplication of the transposed V by V with the normalization of the V. This is shown in Eq. 2.
218

$$S(k_a, k_b) = \frac{\sum_{i=1}^{n} V(i, k_a) V(i, k_b)}{\sqrt{\sum_{i=1}^{n} V(i, k_a)^2} \sqrt{\sum_{i=1}^{n} V(i, k_b)^2}}, \qquad\qquad (2)$$

219

220 where S is the similarity matrix. Each point (k_a, k_b) in S is the cosine similarity between time frame k_a and
221 k_b of V, $\forall k_{a,b} \in [1, m]$, where m is the number of time frames and n is the number of frequency channels
222 for each time frame. Once the similarity matrix is calculated we use it to determine the most similar time
223 frames to each single time frame. For time frame k_a we compare all the values in $S(k_a, k_i)$ for $i \in [1, m]$.
224 We identify similar frames for time frame k_a, by choosing the upper 2% of the all time frames with the
225 highest similarities.
226 Finally, all similar time frames to any frame k in V are stored in a temporary array K. Those similar time
227 frames are used to create a repeating spectrogram model W. The corresponding frame in W is obtained by
228 taking the median of K for each frequency at each time frame k. Those time-frequency bins, which are
229 similar with little deviations between repeating frames, are captured by the median and constitute the
230 repeating spectrogram model. This spectrogram contains only similar and repeating patterns. The time-
231 frequency bins with large deviations between repeating frames would constitute nonrepeating transient
232 patterns and would be suppressed by median filtering.
233
234 The nonnegative spectrogram V is the sum of two nonnegative spectrograms of repeating and nonrepeating

7

235 patterns, hence, W (the repeating spectrogram model) should always have smaller values or at most be
236 equal compared to V. To ensure this, a repeating spectrogram model $\widetilde{W}$ is defined by taking the minimum
237 between W and V. The nonrepeating spectrogram model is derived by subtracting $\widetilde{W}$ from V.
238
239 We use these two (the repeating and the nonrepeating) spectrogram models to create two time-frequency
240 masks for repeating and nonrepeating patterns, respectively. Instead of the binary mask, which is used in
241 Rafii & Pardo (2012), we use soft mask via Wiener filtering (Vaseghi, 1996) which is more flexible and
242 usually leads to a better result. The calculation of the soft masks is shown in the following equations:
243

$$M1 = \frac{\widetilde{W}^2}{\widetilde{W}^2 + \left(V - \widetilde{W}\right)^2}, \tag{3}$$

$$M2 = \frac{\left(V - \widetilde{W}\right)^2}{\left(V - \widetilde{W}\right)^2 + \widetilde{W}^2}, \tag{4}$$

244
245
246 in which $M1$ and $M2$ are repeating and nonrepeating masks respectively. We multiply the masks with the
247 input amplitude spectrogram V to separate the repeating and nonrepeating components. The element-wise
248 multiplication of the masks by the input amplitude spectrogram V is shown in the following equations:
249

$$R = M1 \otimes V, \tag{5}$$

$$NR = M2 \otimes V, \tag{6}$$

250
251 in which R and NR denote repeating and nonrepeating amplitude spectrograms respectively.
252
253 The resulting R and NR spectrograms are shown in Fig. 2a for a specific/typical example of an OBS
254 recording. As can be observed in the R spectrogram, in particular the low frequency harmonic or
255 monochromatic signals below 0.1 Hz are well captured. We applied the SIM algorithm only to the
256 frequency band below 0.1 Hz and above 1 Hz. In the frequency band from 0.1 Hz to 1 Hz the signals
257 remain unchanged by this procedure. This is the first constraint we consider for the SIM algorithm. In the
258 field of noise reduction using signal processing techniques, a very important point is to not modify the
259 signals of interest for analysis. P and S waveforms in the teleseismic earthquake signals have often
260 frequency content in the range of 0.1 Hz to 1 Hz with a dominant frequency around 0.3 Hz. Oceanic
261 microseism noise, which is usually present in the OBS data, has a dominant frequency around 0.1 Hz to 0.3
262 Hz. As P and S phases have similar dominant frequency as the microseism noise wavefield, superposition

263 of both wavefields could happen in this frequency range. They could interfere constructively or

264 destructively so the resulting amplitude could be higher or lower compared to the original P or S phase

265 amplitudes. Considering these interferences, using the SIM algorithm, may result in creating fake higher

266 amplitude for these phases or losing part of their amplitude in the noise reduced signal. But this could be

267 problematic only when the amplitude of the noise is changing over the time. For a noise signal with almost

268 constant amplitude, the SIM algorithm can extract the true amplitude of the noise even in the interference

269 moments. However, the microseism noise has slightly varying amplitude over time.

270

271 Before moving to the second step we introduce a second constraint parameter, which we use in the SIM

272 algorithm. Surface waves of teleseismic events show usually a dispersed narrow-band signal and

273 correspond to mainly horizontal patterns of short duration (on a daily scale) in the spectrogram. Given the

274 way the HPS separates harmonic from transient signals, the surface wavetrain may be erroneously

275 recognized as harmonic component and thus be separated as noise signal. In order to prevent this and

276 preserve the whole frequency content of the earthquake, we define a so-called waiting factor for the

277 similarity calculation introducing a minimum time distance between two consecutive similar frames. For

278 the problem of retaining teleseismic surface waves we found that a waiting factor of at least two hours

279 prevents the algorithm to prune surface waves from the transient signal part. The rationale is that the

280 duration of a teleseismic event is usually less than two hours whereas the noise components have longer

281 duration. Using this waiting factor prevents separating any harmonic component of the earthquake signal as

282 noise component. As a side effect this constraint causes that short-duration harmonic/monochromatic noise

283 signals won't be well captured, too. However, these types of signals are not common in OBS data (see

284 section 2).

285

286 In the second step of our algorithm, to target noise signals in the frequency range of 0.1 Hz to 1 Hz, we use

287 MED as it is described in section 3.2. We apply this second part of the noise removal procedure only to a

288 restricted frequency band of 0.1 Hz to 1 Hz. The dominant noise in the MED frequency range is the

289 current-induced harmonic tremor signal (see section 2).

290 First we create the X' spectrogram which is equal to X in the MED frequency range and is equal to zero

291 outside of this band. Then we apply a horizontal median filter to X' in order to separate harmonic

292 components. This results in the harmonic spectrogram H, which contains near-horizontal patterns captured

293 by the median filter.

294 Now we have two separated spectrograms for noise signals: R, which is derived from the first step, and H,

295 which is derived from the second step. Summing these two spectrograms will build the noise spectrogram

296 N. Subtracting N from the input amplitude spectrogram V will construct the transient spectrogram T.

297 As can be seen in Fig. 2a in step 2, the dominant energy of the narrow-band signals with gliding

298 frequencies in the range of 0.1 Hz to 1 Hz (the current-induced harmonic tremor noise as introduced in the

299 section 2) is captured in the noise spectrogram N, but part of it remains in the transient spectrogram T.

300 Signals with changing frequency which don't form complete horizontal lines in the spectrogram, are
301 difficult to capture by our HPS algorithm, so part of their energy remains in the final spectrogram.
302

303 **3.5 Reconstruction of the denoised signal**
304 In order to reconstruct the noise-removed signal in the time domain we must add phase information to the
305 spectrogram. We had separated the complex-valued spectrogram X into its amplitude V and its phase
306 component using Eq. 1 and all the further modifications have been applied to the amplitude spectrogram V.
307 The phase of input signal SO is mostly affected by the phase of noise signals as they have the dominant
308 energy in the signal. Therefore, we use the phase information of SO in order to reconstruct the noise signal.
309 We add this phase to the noise spectrogram N using the following equation:
310

$$N' = N * exp(1j * \varphi), \qquad (7)$$

311

312 where N' is the complex-valued noise spectrogram. We reconstruct the noise signal NS from the complex
313 spectrogram N', using the inverse STFT. Finally the OBS denoised signal HPS (HPS here represents the
314 SO signal after the HPS processing) is obtained by subtracting the noise signal from the input OBS signal
315 SO using the following equation:
316

$$HPS = SO - NS, \qquad (8)$$

317

318   **3.6 Parameters selection**
319

320 Many typical noise signals observed in OBS recordings are harmonic, monochromatic or narrow-band
321 signals with gliding frequencies (see section 2). In order to extract the expected narrowband noise signals
322 from the STFT we require a high-frequency resolution in the spectral domain, therefore, making it
323 necessary to use sufficiently long time windows for the spectral analysis. Here we use an FFT window
324 length of 163.84 seconds with an overlap of 75%, corresponding to an FFT size of 16384 at a sampling
325 frequency of 100 Hz, which corresponds to a frequency resolution of 0.006 Hz.
326 We use a kernel size of 80 for the median filter in the MED algorithm. The larger the kernel size, the more
327 noise signal would be captured. However, using very large sizes could introduce waveform distortions. As
328 it is discussed in Driedger et al. (2021), the kernel size is not critical as far as not using extreme values. Our
329 tests show that a kernel size of 80 is the largest size, which leads to a safe separation without capturing any
330 energy of the teleseismic signal.
331 The values of parameters, which we used for this study, are presented in Table 1. These are our
332 recommendations for noise reduction of teleseismic earthquakes. One can tune the parameters based on

333   other specific applications such as denoising local earthquakes or extracting specific signals like

334   microseism signal.

335

336   **4 Results and Discussion**

337

338   **4.1 General Results**

339

340   In this section we aim to demonstrate the reliability of our HPS noise reduction algorithm and evaluate the

341   improvement of the OBS data. We applied the method to synthetic and real teleseismic earthquake data

342   recorded by the OBS station D10 of the DOCTAR array (e.g., Hannemann et al, 2016, Hannemann et al.,

343   2017). The synthetics were calculated for a source-receiver epicentral distance of 40° (focal depth: 45 km,

344   focal mechanism: double couple, source duration: 4 s) by using the full wavefield software qseis (Wang,

345   1999) and a modified average ak135 velocity model including a water layer (Kennett et al, 1995). The

346   crustal structure of the velocity model is adapted to the oceanic crust (crustal thickness is 6.6 km) in that

347   area and the water depth is fixed to 4.9 km. Real oceanic noise of the ZRT components recorded by the

348   station D10 is added to the corresponding components of the synthetic teleseismic signal. We created

349   synthetics for three different noise situations at the beginning (N1), during (N2) and after (N3) tidal

350   currents (Fig. 3) each with theoretical SNR of 1–10 between noise and P-onset on pure synthetic Z.

351   Throughout the whole paper the SNR is defined as root mean square (RMS) of the signal divided by RMS

352   of the noise. For further details of synthetic data creation see Fig. S2. For the comparison with real data, we

353   selected in total 46 teleseismic events with magnitudes Mw >5.6 and epicentral distances of 30–160° (see

354   Fig. S1). Here only those events were used, where a P onset could be visually identified. The pre-selection

355   of the events is taken from Hannemann et al. (2017) and expanded by some events with low magnitudes

356   (see Table S1). In the following, we will discuss the improvement of the records by comparing the

357   seismograms and spectrograms of synthetic and real data. We also illustrate the improvement for two

358   seismological applications (teleseismic surface wave group velocity analysis and receiver function

359   analysis). For some observations, e.g. checking the phase arrival of the teleseismic body waves, we rotated

360   the arbitrarily orientated horizontal components of the real data into the ZRT system. The orientation

361   angles are taken from the previous study on the DOCTAR array (Hannemann et al., 2016).

362

363   Comparing the spectrograms and waveforms of the synthetic example we see a significant improvement of

364   SNR in the HPS processed data set on all components (e.g. Fig. 3 and Fig. S3–5 for the real data). The

365   continuous spectral lines of the assumed electronic noise are removed from the data, as well as most of the

366   spectral lines related to tremor episodes of head-buoy strumming. During the tides, we observe a reduction

367   of the spectral amplitudes for the tilt noise, as well as for the general background noise (Fig. 3 and Fig. S3–

368   5) on the horizontal components. The results concluded from the spectrograms are confirmed by the spectra

369   (Fig. 2b), which show the removal of the spectral peaks of the electronic noise (0.05, 0.1, 0.15 Hz) and the

370 tremor episodes (0.5–1 Hz). The amplitude and phase information of the synthetic earthquake are preserved
371 in the HPS signal (see Fig. 3).

372 To quantify the improvements obtained when using our method, we calculated the cross-correlation of
373 the teleseismic waveform, the SNR of the teleseismic body-wave phases and the RMS of the teleseismic
374 waveform before and after denoising. Because most of the oceanic noise ranges at frequencies below 1 Hz,
375 which is also the most interested frequency range of the OBS analysis, a 1 Hz low pass filter is applied to
376 the signals before all result calculations.

377 We calculated the correlation coefficient for synthetic SO and HPS compared with the synthetic earthquake
378 signal for different SNR and noise realizations and plotted it in Fig. 4a. The high correlation coefficients for
379 HPS and synthetic compared with SO and synthetic in all cases demonstrate a significant noise reduction.
380 Furthermore, They indicate that the HPS denoising preserves the earthquake signal and doesn't introduce
381 significant waveform distortions since the HPS is more similar to the synthetics compared to SO. In the
382 following we show other measures that confirm the preservation of the earthquake signal.

383 For the SNR calculation we used a signal window of 30 s starting from the theoretical onset (direct P on Z
384 component, direct S on R and T component and Love wave on the T component) and a noise window of 60
385 s starting 70 s before the theoretical onset. For the Love wave, the SV phase (R component) and P phase (Z
386 component) the SNR increased significantly (Fig. 4b). We find that the noise type properties influence the
387 perceived SNR improvement. It appears that there is no SNR improvement on the T-component for Noise
388 situation N1 (Fig. 4b, the second panel). N1 is taken from the tidal current event's beginning, where there is
389 a significant variation in noise-frequencies over time. In this instance, the signal and noise have comparable
390 frequency ranges. Despite the SNR showing no increase, a visual check of the matching trace reveals a
391 definite improvement in the waveform for the SH-wave on the T component. The results from the cross-
392 correlation (Fig. 4a), confirm the improvement and preservation of the waveform. The SNR should not be
393 utilized alone to assess the improvement by HPS noise reduction approach since we are concentrating on
394 the preservation of the waveform and the SNR comparison strongly depends on the noise situation. The
395 improvement of the traces by the HPS noise reduction approach is confirmed by the study of the cross-
396 correlations, RMS (which is explained in the following paragraph), and the pure waveforms, even though
397 the SNR is not improving in all instances.

398 The RMS amplitudes of a noise-free R component synthetic, SO and HPS signals are estimated over 8
399 seconds windows with 80% overlap and plotted in Fig. 4c. Comparing the RMS amplitude of the synthetic,
400 SO and HPS we see that the synthetic and HPS have similar amplitude ranges while SO has a much higher
401 amplitude. This shows a significant noise reduction in HPS along with preserving the energy of earthquake
402 and all the phase arrivals. As there is some noise remaining after denoising we see some differences in the
403 overall shapes of the RMS amplitude of the synthetic and HPS (especially after minute 24 which is almost
404 at the end of the energy of the synthetic signal). However, HPS shows peaks on the arrival times of seismic
405 phases of the synthetic, which means that the energy of seismic phases is preserved after denoising. The
406 minor changes in seismic phase shapes of the synthetic and HPS are also due to the remaining noise. The

407   seismograms and spectrograms related to this example are presented in Fig. 3. Figure 4d shows a

408   comparison of RMS amplitude of the original noise in SO (blue curve), the remaining noise in HPS after

409   denoising (red curve) and the synthetic earthquake (green curve) signals. Besides a high noise reduction in

410   HPS, the plot shows that the remaining noise is independent of the pattern of the synthetic earthquake,

411   which confirms that the denoising process doesn't affect the earthquake energy in the HPS signal.

412

413   **4.2 Applications**

414   By applying our HPS noise reduction algorithm, we aim to improve seismological analyses, especially

415   those involving the analysis of teleseismic body and surface waves. Valuable constraints of the Earth's

416   structure in oceanic regions can be taken from the analysis of the SH-wavefield like Love-waves, which are

417   not influenced by the water column, but often cannot be analyzed due to strong noise on the horizontal

418   components. SV waves are also often masked by noise, but are for instance important for tomography

419   studies or S and SKS shear wave splitting analysis (e.g. Silver and Chan, 1991). Other techniques using the

420   SV-wavefield like the Z/R ratio of the teleseismic Rayleigh waves (Tanimoto & Rivera, 2008), or receiver

421   functions (RF) (Langston, 1979) also rely on clear radial component readings. In the following we will

422   show the improvement which was achieved for the SH arrivals and for the group velocity analysis of

423   teleseismic Rayleigh- and Love waves, as well as for the receiver function analysis.

424

425   **4.2.1 SH-waves**

426   Since SH-waves are weak in energy and displayed on the noise-contaminated transversal horizontal

427   component (T), they are sparsely observable on OBS recordings and are mostly masked by the high noise

428   level. However, on the HPS processed data we see an improvement of the SNR on the T-component (see

429   Fig. 4b). In many cases the SH-phase is clearly identifiable on the HPS T-component (see Fig. 3d for a

430   synthetic data and Fig. S6 for a real data example).

431

432   **4.2.2 Surface waves**

433   Rayleigh waves in deep oceanic domains are strongly influenced by the water column, because most of the

434   wave energy is traveling in the water. This poses a problem if the water depth changes along the travel

435   path. Love waves are not influenced by the water column but are recorded only on horizontal components

436   and their recordings on OBS systems are therefore more disturbed by strong noise sources like tilt-inducing

437   tidal currents. To test the performance of the HPS noise reduction algorithm in the low frequency range, we

438   performed a measurement of group velocities of Love and Rayleigh waves with the Multiple Filter

439   Technique (MFT) (Dziewonski et al., 1969). Figure 5 shows group velocity curves for the synthetic Love

440   wavetrain for the three noise situations N1-N3. For the MFT analysis we used the software mft96

441   (Herrmann, 2013). The unfiltered seismograms in the top panels (Fig. 5a–c) correspond to the P-wave SNR

442   = 1 scenario. In all three cases the clarity of the dispersion curve is greatly enhanced in the images resulting

443   from the HPS processed traces (Fig. 5e–g) in comparison to the noise free image (Fig. 5d). Also the

444   seismogram traces improved greatly. The dispersion images show how noise energy is successfully

445   removed from the frequency range of 0.05 to 0.2 Hz, which is the event frequency range. Lower frequency

446   range which are weakly visible in the noise-free image (Fig. 5d) can not be recovered. The corresponding

447   results for the Rayleigh wavetrain on the radial component are shown in Fig. S7. For the N3 case here also

448   low frequency range down to 0.025 Hz can be successfully denoised.

449   For an evaluation of the HPS denoising technique on real surface wave data we selected 23 events with

450   magnitudes larger than Mw 6.0 in the distance range between 47.5° and 159.6° and added one event with

451   Mw= 5.6 at a distance of 37.9° (see Fig. S1). Figure S8 shows seismograms and MFT analysis examples

452   for three events with different magnitudes and in different distances. The resulting group velocity

453   dispersion curves for all 24 events for the original and processed data are shown in Fig. S9. For all

454   components we find that the improved signal to noise ratio of the processed data allows the analysis of

455   more events and of a broader frequency range than in the original data.

456   **4.2.3 Receiver Functions**

457   Receiver functions have been proven to be a valuable tool to observe the Earth's structure using teleseismic

458   events (e.g., Langston, 1979, Ammon et al., 1995, Kind et al., 1995; Rondenay, 2009). Separating the

459   source site from the receiver site by deconvolution allows to estimate the Earth's structure beneath the

460   station. Here, we compare the receiver functions calculated from the synthetic examples and from real data

461   before and after denoising (Fig. 6). The synthetics used for the receiver function calculation are pure

462   synthetic signals contaminated by real noise (N1, N2, N3). On the synthetics, the SNR for P ranges

463   between 1–10 (for detailed description of the synthetic creation, see section 4.1, Fig. 3 and S2). Receiver

464   function analysis and the observation of the Earth's structure beneath the DOCTAR array was already

465   calculated by Hannemann et al. (2017). Here, we don't aim to estimate the crustal and mantle structures,

466   instead we aim to compare the P-receiver Functions of the radial component calculated from the original

467   synthetic and real data (SO R-RF) with receiver functions of the radial component from the HPS processed

468   synthetic and real data (HPS R-RF). To calculate the receiver functions, we applied the iterative

469   deconvolution in the time domain (Ligorría & Ammon, 1999). We corrected the data for the Ps-phase,

470   quality controlled (e.g. P-onset at 0 s on Z of HPS R-RF), stacked and low-pass filtered the synthetic data at

471   2 Hz and bandpass filtered the traces between 0.05–0.5 Hz for the real data with a zero-phase Butterworth

472   filter. For both synthetic and real receiver function, the noise level strongly decreased and we observe a

473   significant decrease in variance on the HPS traces compared to the SO traces (Fig. 6).

474   Our result shows that determination of the crustal- and mantle-phases is more reliable on the HPS R-RF

475   stack than on the SO R-RF stack for both synthetic and real data (Fig. 6). We observe more distinct Ps-

476   phase arrivals on the HPS R-RF than on the SO R-RF stack. The Ps-phases are caused by the P-to-S

477   conversion at the Mohorovičić-, 410-km and 660-km discontinuity (hereafter referred to as Moho, 410, and

478   660, respectively; e.g. Deuss, 2009). For the synthetic example, we expect the P-to-s conversion at the

479   Moho at depths of 11.5 km to arrive at 0.8s, which is better resolved in the synthetic HPS R-RF than in the

480   synthetic SO R-RF, same for it's multiple (P_MsPp) and the water multiples every 6.5s (M_{WATER}, Fig. 6a).

481   Assuming ak135 velocities we would expect the $P_{410}s$-phase (Ps conversion at the 410) to arrive at around

482   43 s and the $P_{660}s$-phase (Ps conversion at the 660) at around 66.8 s delayed to the direct P-arrival (see Fig.

483   6 a & b).

484

485   Instead of a rather weak peak on the SO-R-RF real data stack we observe a strong peak at around 43 s, with

486   a good SNR on the HPS R-RF stack, indicating the sharp velocity contrast at the 410 (Fig. 6b). Comparing

487   SO-RF and HPS-RF real data stacks, the amplitudes of the P660s-phase on the HPS decreased and became

488   a broader peak. This aligns with our expectations from a conversion at a gradual velocity contrast as at the

489   660. These results are in line with the analysis of the crustal and mantle structure beneath the DOCTAR

490   array presented by Hannemann et al. (2017). The negative phase (X1 in Fig. 6b) arriving at around 5 s is

491   stronger on the HPS-R-RF real data stack than on the SO-R-RF real data stack and might either indicate the

492   PpSs multiple of the Ps-phase at the Moho, or the direct P-to-s conversion at the LAB. On the HPS-R-RF

493   real data stack we observe a strong positive phase (X2) arriving at 12 s (Fig. 6b). This phase has not been

494   identified by Hannemann et al. (2017) and a detailed analysis of its origin is beyond the scope of this study,

495   but it might be related to the water multiples.

496

497   **5 Conclusions**

498

499   In this work we have developed a method to separate the signals of teleseismic earthquakes from other

500   signals in OBS recordings resulting in noise reduction of OBS data. Our method is a combination of two

501   HPS algorithms from the field of music information retrieval (MIR) to separate harmonic and percussive

502   components of OBS data. Earthquake signals as percussive components are separated from noise signals as

503   harmonic components. The noise signal is reconstructed using the phase information of the original signal.

504   Subtracting the noise signal from the original signal derives the noise-reduced signal. Our two-step HPS

505   approach results in a cleaner, noise-reduced signal where the teleseismic broadband earthquake waveforms

506   are preserved with their whole frequency content. Our synthetic tests shows that the SNR of HPS noise

507   reduced signal significantly increases in most cases, however, the apparent SNR improvement depends on

508   the noise type characteristics. The type of noise signals, which are eligible for our noise reduction

509   algorithm, contains most of the OBS noise energy.

510   The extracted noise signal contains some different signals where each can be derived by applying a band

511   pass filter to the extracted noise signal in a proper frequency band. The derived signal may be used in

512   researches related to that signal. For example the microseism signal can be extracted and used for

513   investigation of the source generation area of microseisms.

514   From our analysis of the broadband seismograms, we find out that the improvement is significant and

515   allows a broader and more reliable analysis of teleseismic earthquake data. Applications like the receiver

516   function technique and SH-wave and Love wave analysis are considerably improved after applying the

517   HPS noise reduction algorithm.

Group velocity analysis of teleseismic surface wavetrains showed that application of the HPS noise reduction technique allows to analyze more events and to analyze them in a broader frequency range. Especially more and wider Love wave dispersion curves could be recovered. The noise reduction algorithm improves the horizontal components significantly, which allows the OBS community to apply a broader range of seismological methodologies, including the horizontal components, to the OBS-data.

Code and data availability

A Python package named NoiseCut (Zali, 2022) and the code related to the proposed method along with an example of real data is freely available from https://github.com/ZahraZali/NoiseCut. The average computation time for this example (one day OBS signal with a sampling frequency of 100 Hz) is about 7 minutes on a PC with an Intel core i7 (six-core) processor of 2.2 GHz and 16 GB of RAM. A Jupyter notebook with all the Python codes and parameters related to the proposed method is available as an electronic supplement. The sea floor seismological data were archived by Alfred Wegener Institute (AWI), Helmholtz Centre for Polar Research, Bremerhaven, Germany, and are available upon request. The supplementary material related to this article contains list of all earthquakes used in this study and a map showing their location. The illustrations of the semi-synthetic data generation are presented in the supplementary material as well. An example of three components seismogram and spectrogram before and after applying HPS noise reduction algorithm to real data, Rayleigh wave group velocity analysis for a synthetic example, MFT analysis for three real events and group velocity curves for some real events are also presented through figures in the supplementary material.

Author contribution

Z.Z. developed the algorithm and designed the study. T.R. created the synthetics data, conducted the synthetic tests, and measured the receiver functions. F.K. conducted the group velocity analysis. Z.Z., T.R., and F.K. evaluated the results. Z.Z. and T.R. wrote the initial draft. All authors wrote the final manuscript and discussed the results.

Competing interests

The authors declare that they have no conflict of interest.

553   Institut Helmholtz-Zentrum für Polar- und Meeresforschung et al., 2017) that is currently the largest

554   European OBS pool. We acknowledge Sebastian Heimann for helping in packaging of the code related to

555   the method. For building our method, we used Librosa, a Python package for audio and music signal

556   processing (McFee et al., 2020). The data processing was done using obspy (Beyreuther et al., 2010) and

557   pyrocko (Heimann et al., 2017); the receiver functions were calculated using the rf-package (Eulenfeld,

558   2020).

559

560   **References**

561   Alfred-Wegener-Institut, Helmholtz-Zentrum für Polar- und Meeresforschung et al.: DEPAS (Deutscher

562   Geräte-Pool für amphibische Seismologie): German Instrument Pool for Amphibian Seismology, J.

563   Largescale Res. Facil., 3, A122, https://doi.org/10.17815/jlsrf-3-165, 2017.

564

565   Ammon, C. J., Randall, G. E., & Zandt, G.: On the nonuniqueness of receiver function inversions, J.

566   Geophys. Res.-Sol. Ea., 95(B10), 15303-15318, https://doi.org/10.1029/JB095iB10p15303, 1990.

567

568   An, C., Cai, C., Zhou, L., & Yang, T.: Characteristics of Low-Frequency Horizontal Noise of Ocean-

569   Bottom Seismic Data, Seismol. Res. Lett., https://doi.org/10.1785/0220200349, 2021.

570

571   Bell, S. W., Forsyth, D. W., & Ruan, Y.: Removing noise from the vertical component records of ocean-

572   bottom seismometers: Results from year one of the Cascadia Initiative, B. Seismol. Soc. Am., 105(1), 300-

573   313, https://doi.org/10.1785/0120140054, 2015.

574

575   Beyreuther, M., Barsch, R., Krischer, L., Megies, T., Behr, Y., Wassermann, J.: ObsPy: A Python

576   Toolbox for Seismology. Seismol. Res. Lett., 81(3), 530-533, 2010.

577   Brink, K. H.: Tidal and lower frequency currents above Fieberling Guyot. J. Geophys. Res.-:

578   Oceans, 100(C6), 10817-10832, https://doi.org/10.1029/95JC00998, 1995.

579

580   Corela, C.: Ocean bottom seismic noise: applications for the crust knowledge, interaction ocean-

581   atmosphere and instrumental behaviour. Ph.D. thesis, University of Lisbon, 339 pp, 2014.

582

583   Crawford, W. C.: Determination of oceanic crustal shear velocity structure from seafloor compliance

584   measurements (Doctoral dissertation, University of California, San Diego), 1994.

585

586   Crawford, W. C., & Webb, S. C.: Identifying and removing tilt noise from low-frequency (< 0.1 Hz)

587   seafloor vertical seismic data. B. Seismol. Soc. Am., 90(4), 952-963, https://doi.org/10.1785/0119990121,

588   2000.

589

590 Crawford, W. C., Webb, S. C., & Hildebrand, J. A.: Estimating shear velocities in the oceanic crust from
591 compliance measurements by two-dimensional finite difference modeling. J. Geophys. Res.-Sol. Ea.,
592 103(B5), 9895-9916, https://doi.org/10.1029/97JB03532, 1998.

594 Deuss, A.: Global observations of mantle discontinuities using SS and PP precursors. Surv.
595 Geophys., 30(4-5), 301-326, https://doi.org/10.1007/s10712-009-9078-y, 2009.

597 Driedger, Jonathan, Meinard Müller, and Sascha Disch. "Extending Harmonic-Percussive Separation of
598 Audio Signals." In ISMIR, pp. 611-616. 2014.

600 Duennebier, F. K., & Sutton, G. H.: Fidelity of ocean bottom seismic observations, Oceanographic
601 Literature Review, 10(43), 996, https://doi.org/10.1007/BF01204343, 1995.

603 Dziewonski, A., S. Bloch, and M. Landisman.: A technique for the analysis of transient seismic signals, B.
604 Seismol. Soc. Am., 59, no. 1, 427-444, https://doi.org/10.1785/BSSA0590010427, 1969.

606 Essing, D., Schlindwein, V., Schmidt-Aursch, M. C., Hadziioannou, C., & Stähler, S. C.: Characteristics of
607 Current-Induced Harmonic Tremor Signals in Ocean-Bottom Seismometer Records, Seismol. Res.
608 Lett., 92(5), 3100-3112. , https://doi.org/10.1785/0220200397, 2021.

610 Eulenfeld, T.: rf: Receiver function calculation in seismology, Journal of Open Source Software, 5(48),
611 1808, https://doi.org/10.21105/joss.01808, 2020.

613 Fitzgerald, D.: Harmonic/percussive separation using median filtering, In Proceedings of the International
614 Conference on Digital Audio Effects (DAFx) (Vol. 13), 2010.

616 FitzGerald, D.: Vocal separation using nearest neighbours and median filtering, 23rd IET Irish Signals and
617 Systems Conference, Maynooth. 28-29th. June 2012, https://doi.org/10.1049/ic.2012.0225, 2012.

619 Friedrich, A., Krüger, F., & Klinge, K.: Ocean-generated microseismic noise located with the Gräfenberg
620 array, J. Seismol., 2(1), 47-64, https://doi.org/10.1023/A:1009788904007, 1998.

622 Gaspà Rebull, O., Cusí, J. D., Ruiz Fernández, M., & Muset, J. G.: Tracking fin whale calls offshore the
623 Galicia Margin, north east Atlantic Ocean, The Journal of the Acoustical Society of America, 120(4), 2077-
624 2085, https://doi.org/10.1121/1.2336751, 2006.

626 Griffin, O. M.: Vortex-Induced Vibrations of Marine Cables and Structures, NRL Memorandum Report
627 5600, Naval Research Laboratory – Marine Technology Division, Washington D.C, 1985.

628

629 Hannemann, K., Krüger, F., Dahm, T., & Lange, D.: Structure of the oceanic lithosphere and upper mantle

630 north of the Gloria fault in the eastern mid-Atlantic by receiver function analysis, J. Geophys. Res-Sol Ea.,

631 122(10), 7927-7950, https://doi.org/10.1002/2016JB013582, 2017.

632

633 Hasselmann, K.: A statistical analysis of the generation of microseisms. Rev. Geophys., 1(2), 177-210,

634 https://doi.org/10.1029/RG001i002p00177, 1963.

635

636 Heimann, S., Kriegerowski, M., Isken, M., Cesca, S., Daout, S., Grigoli, F., Juretzek, C., Megies, T.,

637 Nooshiri, N., Steinberg, A., Sudhaus, H., Vasyura-Bathke, H., Willey, T., Dahm, T.: Pyrocko - An open-

638 source   seismology   toolbox   and   library.   V.   0.3.   GFZ   Data   Services,

639 https://doi.org/10.5880/GFZ.2.1.2017.001, 2017.

640

641 Herrmann, R. B.: Computer programs in seismology: An evolving tool for instruction and research, Seism.

642 Res. Lettr., 84, 1081-1088, https://doi.org/10.1785/0220110096, 2013.

643

644 Janiszewski, H. A., Gaherty, J. B., Abers, G. A., Gao, H., & Eilon, Z. C.: Amphibious surface-wave phase-

645 velocity measurements of the Cascadia subduction zone. Geophys. J. Int., 217(3), 1929-1948,

646 https://doi.org/10.1093/gji/ggz051, 2019.

647

648 Johnson, J. B., & Watson, L. M.: Monitoring volcanic craters with infrasound "music", Eos, 100.

649 https://doi.org/10.1029/2019EO123979, 2019.

650

651 Kennett, B. L., Engdahl, E. R., & Buland, R.: Constraints on seismic velocities in the Earth from

652 traveltimes. Geophys. J. Int., 122(1), 108-124, https://doi.org/10.1111/j.1365-246X.1995.tb03540.x, 1995.

653

654 Kind, R., Kosarev, G. L., & Petersen, N. V.: Receiver functions at the stations of the German Regional

655 Seismic Network (GRSN). Geophys. J. Int., 121(1), 191-202, https://doi.org/10.1111/j.1365-

656 246X.1995.tb03520.x, 1995.

657

658 Langston, C.A.: Structure under Mount Rainier, Washington, inferred from teleseismic body waves. J.

659 Geophys. Res., 84, 4749-4762, https://doi.org/10.1029/JB084iB09p04749, 1979.

660

661 Ligorría, J. P., & Ammon, C. J.: Iterative deconvolution and receiver-function estimation. B. Seismol. Soc.

662 Am., 89(5), 1395-1400, https://doi.org/10.1785/BSSA0890051395, 1999.

663

664   Longuet-Higgins, M. S.: A theory of the origin of microseisms, Philosophical Transactions of the Royal

665   Society of London. Series A, Mathematical and Physical Sciences, 243(857), 1-35,

666   https://doi.org/10.1098/rsta.1950.0012, 1950.

667

668   McFee, B., V. Lostanlen, A. Metsai, M. McVicar, S. Balke, C. Thomé, C. Raffel, F. Zalkow, A. Malek,

669   Dana, et al.: librosa/librosa: 0.8.0, Version 0.8.0, Zenodo, https://doi.org/10.5281/zenodo.3955228, 2020.

670

671   Mousavi, S. M., & Langston, C.A.: Automatic noise-removal/signal-removal based on general cross-

672   validation thresholding in synchrosqueezed domain and its application on earthquake data. Geophysics,

673   82.4, V211-V227. https://doi.org/10.1190/geo2016-0433.1, 2017.

674

675   Müller, M.: Fundamentals of music processing: Audio, analysis, algorithms, applications. Cham,

676   Switzerland: Springer International Publishing. https://doi.org/10.1007/978-3-319-21945-5, 2015.

677

678   Negi, S. S., Kumar, A., Ningthoujam, L. S., & Pandey, D. K.: An Efficient Approach of Data Adaptive

679   Polarization Filter to Extract Teleseismic Phases from the Ocean-Bottom Seismograms. Seismological

680   Society of America, 92(1), 528-542, https://doi.org/10.1785/0220200034, 2021.

681

682   Olofsson, B.: Marine ambient seismic noise in the frequency range 1–10 Hz. The Leading Edge, 29(4),

683   418-435, https://doi.org/10.1190/1.3378306, 2010.

684

685   Pereira, A., Romagosa, M., Corela, C., Silva, M. A., & Matias, L.: Source Levels of 20 Hz Fin Whale

686   Notes Measured as Sound Pressure and Particle Velocity from Ocean-Bottom Seismometers in the North

687   Atlantic. Journal of Marine Science and Engineering, 9(6), 646, https://doi.org/10.3390/jmse9060646,

688   2021.

689

690   Pillet, R., Deschamps, A., Legrand, D., Virieux, J., Béthoux, N., & Yates, B.: Interpretation of broadband

691   ocean-bottom seismometer horizontal data seismic background noise, B. Seismol. Soc. Am., 99(2B), 1333-

692   1342, https://doi.org/10.1785/0120080123, 2009.

693

694   Rafii, Z., Liutkus, A., & Pardo, B.: REPET for background/foreground separation in audio. In Blind Source

695   Separation (pp. 395-411). Springer, Berlin, Heidelberg, https://doi.org/10.1007/978-3-642-55016-4_14,

696   2014.

697

698   Rafii, Z., Liutkus, A., Stöter, F. R., Mimilakis, S. I., FitzGerald, D., & Pardo, B.: An overview of lead and

699   accompaniment separation in music, IEEE/ACM Transactions on Audio, Speech, and Language

700   Processing, 26(8), 1307-1335. https://doi.org/10.1109/TASLP.2018.2825440, 2018.

701

702 Rafii, Z., & Pardo, B.: Music/Voice Separation Using the Similarity Matrix, Proc. ISMIR, pp. 583-588,
703 2012.

704

705 Ramakrushana Reddy, T., Dewangan, P., Arya, L., Singha, P., & Kamesh Raju, K. A.: Tidal triggering of
706 the harmonic noise in ocean-bottom seismometers. Seismol. Res. Lett., 91(2A), 803-813,
707 https://doi.org/10.1785/0220190080, 2020.

708

709 Rondenay, S.: Upper mantle imaging with array recordings of converted and scattered teleseismic waves.
710 Surv. Geophys., 30(4), 377-405, https://doi.org/10.1007/s10712-009-9071-5, 2009.

711

712 Romanowicz, B., Stakes, D., Montagner, J. P., Tarits, P., Uhrhammer, R., Begnaud, M., Stutzmann, E.,
713 Pasyanos, M., Karczewski, J.F., Etchemendy, S. and Neuhauser, D.: MOISE: A pilot experiment towards
714 long term sea-floor geophysical observatories, Earth, planets and space, 50(11), 927-937,
715 https://doi.org/10.1186/BF03352188, 1998.

716

717 Schlindwein, V., Krüger, F., Schmidt-Aursch, M.: Project KNIPAS: DEPAS ocean-bottom seismometer
718 operations in the Greenland Sea in 2016-2017, Alfred Wegener Institute, Helmholtz Centre for Polar and
719 Marine Research, Bremerhaven, PANGAEA, https://doi.org/10.1594/PANGAEA.896635, 2018.

720

721 Schlindwein, V., Wassermann, J., & Scherbaum, F.: Spectral analysis of harmonic tremor signals at Mt.
722 Semeru volcano, Indonesia, Geophys. Res. Lett., 22(13), 1685-1688. https://doi.org/10.1029/95GL01433,
723 1995.

724

725 Skop, R. A., & Griffin, O. M.: On a theory for the vortex-excited oscillations of flexible cylindrical
726 structures. Journal of Sound and Vibration, 41(3), 263-274, https://doi.org/10.1016/S0022-460X(75)80173-
727 8, 1975.

728

729 Silver, P.G. & Chan, W.W.: Shear wave splitting and subcontinental mantle deformation. J. Geophys. Res.,
730 96, 16429-16454, https://doi.org/10.1029/91JB00899, 1991.

731

732 Snodgrass, F. E., Hasselmann, K. F., Miller, G. R., Munk, W. H., & Powers, W. H.: Propagation of ocean
733 swell across the Pacific, Philosophical Transactions of the Royal Society of London. Series A,
734 Mathematical and Physical Sciences, 259(1103), 431-497, https://doi.org/10.1098/rsta.1966.0022, 1996.

735

736 Stähler, S. C., Schmidt-Aursch, M. C., Hein, G., & Mars, R.: A self-noise model for the German DEPAS
737 OBS pool. Seismol. Res. Lett., 89(5), 1838-1845, https://doi.org/10.1785/0220180056, 2018.
738

739 Tanimoto, T., Rivera, L.: The ZH ratio method for long-period seismic data: sensitivity kernels and
740 observational techniques. Geophys. J. Int., 172(1), 187-198, https://doi.org/10.1111/j.1365-
741 246X.2007.03609.x, 2008.
742

743 Titze, I. R.: Nonlinear source–filter coupling in phonation: Theory, The Journal of the Acoustical Society
744 of America, 123(4), 1902-1915, https://doi.org/10.1121/1.2832337, 2008.
745

746 Vaseghi, S. V.: Advanced signal processing and digital noise reduction. Vieweg + Teubner Verlag,
747 https://doi.org/10.1002/9780470740156, 1996.
748

749 Wang, R.: A simple orthonormalization method for stable and efficient computation of Green's
750 functions, B. Seismol. Soc. Am., 89(3), 733-741, https://doi.org/10.1785/BSSA0890030733, 1999.
751

752 Webb, S. C.: Broadband seismology and noise under the ocean, Rev. Geophys., 36(1), 105-142,
753 https://doi.org/10.1029/97RG02287, 1998.
754

755 Webb, S. C., Zhang, X., & Crawford, W.: Infragravity waves in the deep ocean, J. Geophys. Res.-:
756 Oceans, 96(C2), 2723-2736, https://doi.org/10.1029/90JC02212, 1991.
757

758 Zahra Zali. (2022). ZahraZali/NoiseCut: NoiseCut (v1.0.0). Zenodo.
759 https://doi.org/10.5281/zenodo.7339552
760

761 Zali, Z., Ohrnberger, M., Scherbaum, F., Cotton, F., & Eibl, E. P.: Volcanic Tremor Extraction and
762 Earthquake Detection Using Music Information Retrieval Algorithms, Seismol. Res. Lett., 92(6), 3668-
763 3681, https://doi.org/10.1785/0220210016, 2021.
764

765 Zhu, W., Mousavi, S. M., & Beroza, G. C.: Seismic signal denoising and decomposition using deep neural
766 networks. IEEE T. Geosci. Remote., 57(11), 9476-9488. https://doi.org/10.1109/TGRS.2019.2926772,
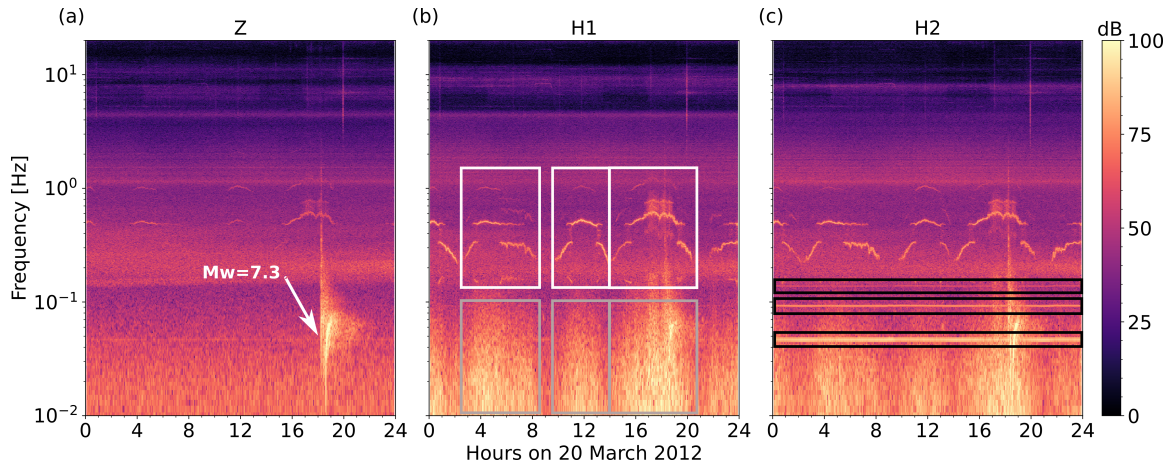767 2019.
768

769

770

Figure 1: Spectrogram of an one-day OBS signal shows ocean bottom noise on Z (a), H1 (b) and H2 (c) components. The data was recorded by the station D10 of the DOCTAR array with a sampling frequency of 100 Hz. The spectrogram were calculated using a window length of 2^{16} sample and an overlap of 75%. The signal of an earthquake (Mw=7.3) on 20.3.2012 at around 18:00 at the station D10 is shown in (a). The tidal cycle of the current-induced noise is clearly visible during the high tilt noise episodes (gray box in b). The white box in (b) highlights the tremor episodes caused by the head buoy strumming. On H2 (c) we see an instrument-related, presumably electronic noise (black boxes). The high energy of the secondary microseism band at around 0.2 Hz is visible on all components.
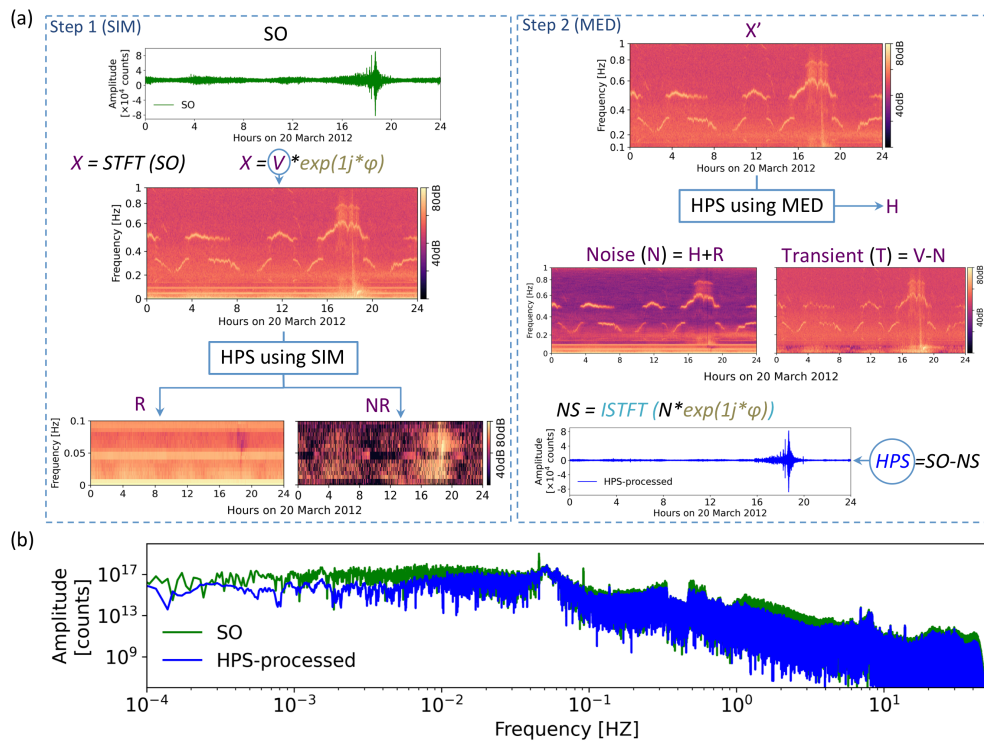
Figure 2: Method flowchart (a) Illustration of the processing steps with a real data example. Left panel shows the first step of the method where using the similarity matrix (SIM) in the frequency range below 0.1 Hz and above 1 Hz, we divide the spectrogram (X) of the original signal (SO) into two spectrograms of repeating (R) and non-repeating (NR) patterns. Right panel shows the second step of the method where we apply a median filter (MED) to the frequency range of 0.1 to 1 Hz (spectrogram X') in order to remove noises from this frequency range. It results in the harmonic spectrogram (H). As the interested frequency range for OBS signals is below 1 Hz, the spectrograms show only this frequency range. Finally the noise spectrogram (N) is created by summing the separated noises derived from two steps and the noise signal (NS) is derived using ISTFT. We obtain the noise reduced signal (HPS) by subtracting the NS from the input OBS signal (SO). STFT, short time Fourier transform. HPS, harmonic-percussive separation. SIM, similarity matrix. MED, median filtering. ISTFT, Inverse Short Time Fourier Transform. (b) Spectrum of the original signal (SO) and the HPS noise reduced signal.
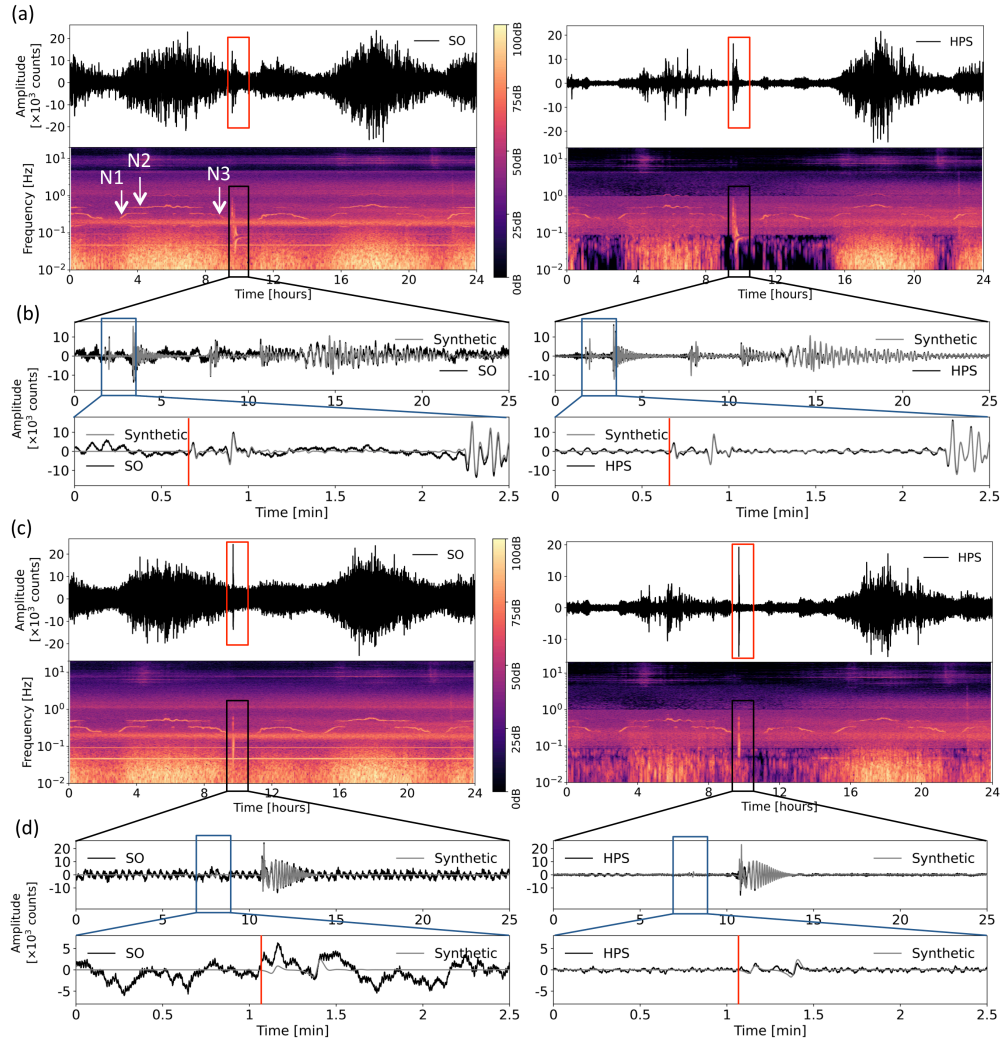
Figure 3: Comparison of the synthetic seismograms and spectrograms of the original signal SO and the HPS noise reduced signal on the R and T components for a synthetic signal with SNR= 1.5 before denoising. (a) & (c) Show one day seismograms and spectrograms for R and T components, respectively. Squares show the earthquake section. The arrows in (a) show three noise situations (N1-N3). (b) & (d) Show seismograms of the earthquake section on SO and HPS signals, with detailed view of the P-arrival (on component R in subfigure b) and SH-arrival (on component T in subfigure d). Red lines show P-arrivals in (b) and SH-arrival in (d).
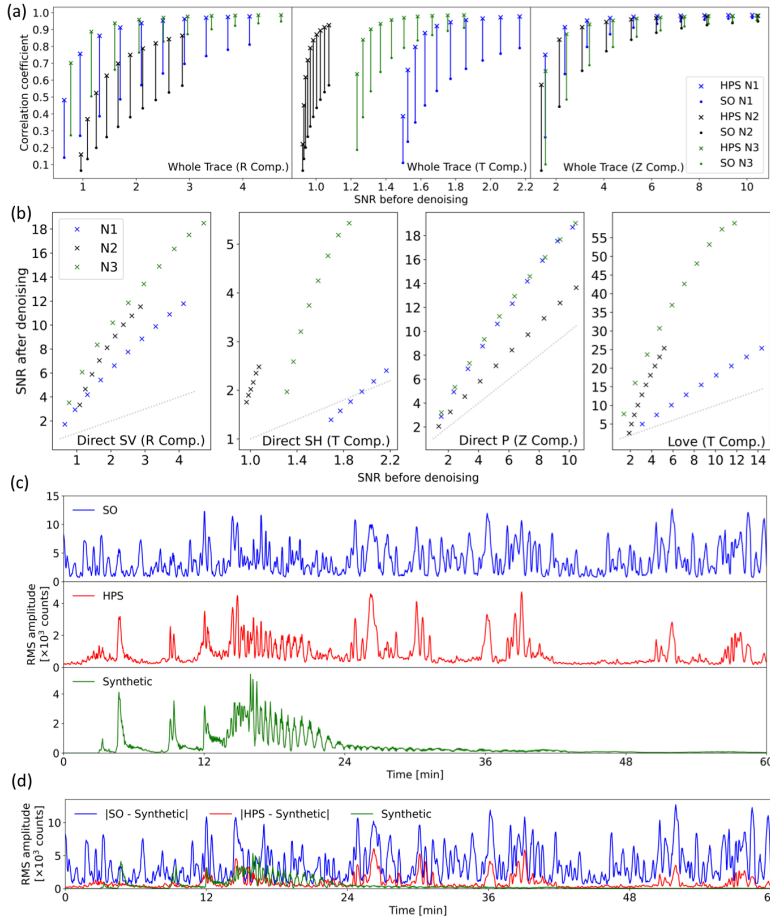
807
808
809 **Figure 4: Comparison of the synthetic SO and HPS signals (both are lowpass filtered at 1Hz). (a) Correlation**
810 **coefficients (for the whole trace) for different SNRs and 3 realistic noise realizations for Z, R and T components**
811 **(Component is abbreviated as Comp.). (b) Improvement of SNR for direct body wave phases and the Love wave.**
812 **The gray dotted lines in (b) mark the line with gradient 1 (no improvement of SNR). (c) Comparison of the root**
813 **mean square (RMS) amplitude of one example of the SO, HPS and synthetic earthquake signals. This signal is**
814 **the same example shown in Fig. 3 (R component, SNR= 1.5 before denoising). (d) The RMS of the original noise**
815 **(blue trace: |SO - Synthetic|) and the remained noise after denoising (red trace: |HPS- Synthetic|) compared to**
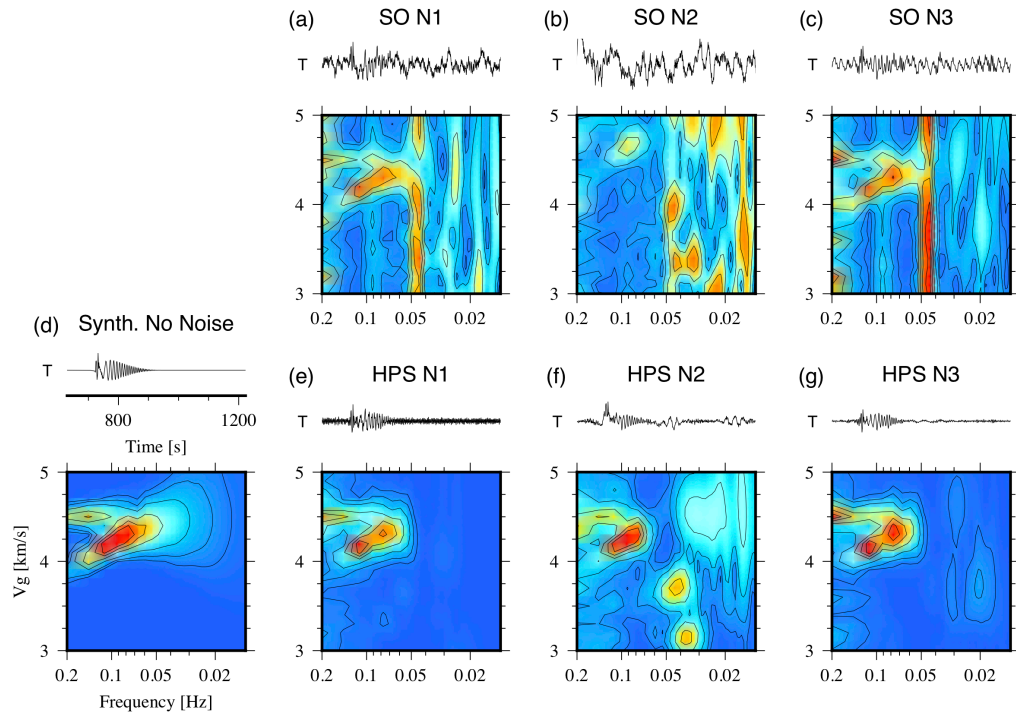816 **the synthetic earthquake signal.**
817

Figure 5: Love wave group velocity analysis for unfiltered and HPS processed synthetic Love wavetrains contaminated by three real world OBS noise signals (noise situations N1-N3, station D10, DOCTAR experiment, see section 2 for more details). (a)–(c): Lower panels: Unfiltered synthetic signal (SO) MFT analysis results. Top panels: seismogram time windows corresponding to the range of group velocities shown on the y-axis. (d) Noise free synthetic case. (e)–(g): HPS processed input traces for noise situations N1-N3 (lower panel: MFT analysis result, top panel: HPS processed seismogram).
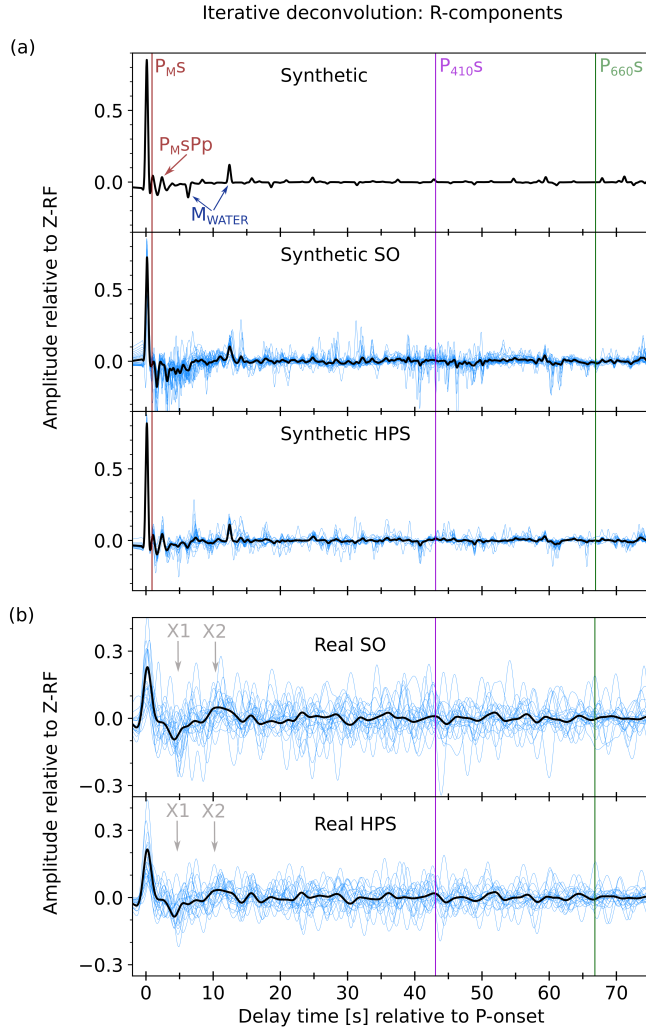
Figure 6: R-receiver function comparison of synthetic and real data examples. (a) Comparison of the synthetic data examples, lowpass filtered at 2 Hz. The pure synthetic R-RF is shown in the uppermost panel, followed by the synthetic SO and the synthetic HPS R-RFs. The black lines show the summed individual R-RFs (blue waveforms). The theoretical onset times for this specific model are marked. Red line: Ps-arrival of the Moho (P_MS) and its multiple (P_MsPp), violet line: Ps arrival of the 410 ($P_{410}s$), green line: Ps-arrival of the 660 ($P_{660}s$), dark-blue arrows: Multiples in the watercolumn of 4.9 km (M_{WATER}), repetitive every 6.5s. (b) Comparison of the real data, bandpass filtered at 0.05–0.5 Hz. The upper panel shows the R-RFs of the real SO traces and the lowermost panel the R-RFS of the real HPS traces. The individual traces (blue) are shown as stack (black line) and the theoretical onset times based on the average ak135 velocity model are shown as violet line ($P_{410}s$) and green line ($P_{660}s$). The origin of the phases X1 and X2 (gray) remain unclarified, since their interpretation is beyond the scope of this study.

838 **Table 1: Parameters values used in our study**

Parameters	FFT window size	FFT overlapping percentage	SIM frequency range	SIM waiting factor	SIM upper threshold	MED frequency range	MED kernel size
Values	16384 samples	75%	[0-0.1] & above 1 Hz	2 hours	2%	[0.1-1] Hz	80

839